Size-selective and facile synthesis of ZnO/ZnS core–shell nanostructure and its characterization

G. Swati[1] · Manoj Morampudi[2]

Abstract

A novel methodology and its mechanism to synthesize ZnO/ZnS core–shell nanostructure by hydrothermal-supported co-precipitation method are presented. Chemical precursors Na_2S and thioacetic acid were used as chemical conversion agents. Detailed structural, morphological, compositional and optical studies were carried out. Powder X-ray diffraction analysis confirms the presence of both wurtzite and cubic phase in ZnO/ZnS core–shell, respectively. OH absorption capacity of as-grown ZnO/ZnS nanostructures was found to be enhanced due to interfacial roughness ZnO/ZnS as compared to pristine ZnO. Morphological studies confirm the formation of irregular spherical nanocrystals of size ~ 50 nm. Band gap of ZnO nanocrystals was found to be increased upon sulphidation process. Room temperature EPR studies also confirmed the ZnS shell over ZnO nanocrystals suppresses the paramagnetic defects in ZnO. Interestingly, defect-related visible light emission from ZnO nanocrystals was found to be suppressed completely due to the presence of the larger band gap of ZnS as a shell over ZnO core. ZnS shell restricts the photogenerated charge carriers within the ZnO nanocrystal core, making ZnO/ZnS core–shell a potential candidate for optoelectronic applications such as UV photodetectors.

Keywords Core–shell · Photoluminescence · Semiconductors

1 Introduction

Owing to a high surface-to-volume ratio in nanocrystals, the surface acts as a new state of matter; thus, surface engineering of nanocrystals becomes a prerequisite towards developing stable nanocrystals for any practical applications [1–4]. One of the interesting approaches to develop stable semiconductor nanocrystals is developing core–shell semiconducting structures. Core/shell structures show fascinating optoelectronic, electrochemical and magnetic properties as compared to their pristine individual components. Zinc oxide is a metal oxide semiconductor with wide near UV excitable band gap energy, high exciton binding energy (~60 meV) and large molar absorption coefficient because of which Zinc oxide finds a diverse application in the field of light-emitting diodes, excimer lasers, photovoltaics, nonlinear optical devices, UV photodetectors, electroluminescent panels, transparent conducting electrodes photocatalysis and plasmonics [5–13]. Strong near UV emission from zinc oxide (ZnO) makes it an emerging alternative semiconductor material to gallium nitride. However, a strong broadband greenish yellow emission due to intrinsic and extrinsic defects in zinc oxide inhibits widespread application of ZnO for various optoelectronic applications such as varistors, UV-emitting diodes, ultraviolet detectors and diode lasers. [14, 15]. Defects states were also found to reduce the piezoelectric voltage obtained from ZnO nanocrystals by screening the polarization charges. To deal with the issue, researchers across the globe are investigating ways to eradicate parasitic defect states from semiconducting nanocrystals such as surface passivation using surfactants, organic ligands and polymers, high-temperature annealing and doping [16–19].

Parasitic defect states from ZnO nanocrystals attribute to zinc interstitial and oxygen vacancy-related unwanted defects which may creep up during preparation and annealing conditions. Thus, carefully selecting the synthesis procedure is one of the crucial steps that govern the role of defects in ZnO [20]. One of the most intriguing methods towards eliminating the defect-related emission is effective surface modification

✉ G. Swati
  swati.g@vit.ac.in

[1] Centre for Nanotechnology Research, Vellore Institute of Technology, Vellore 632014, India

[2] Department of Electrical and Electronic Engineering, Ganga Institute of Technology and Management, Jhajjar, India

via creating core–shell nanostructure which are composed of the semiconducting core material and a shell of a dissimilar semiconducting material [21, 22]. Also, the semiconducting shell acts as a mechanical shield between the optically responsive core and the surrounding external environment, thereby defending core towards environmental changes such as photo-oxidation [24–28]. In a study by Liqiao Qin et al., surface of ZnO nanoparticles was treated by polyvinyl alcohol to enhance UV emission and a stable dispersion of ZnO nanoparticles. Photoconductors fabricated using the PVA-coated zinc oxide nanoparticles were found to have ratio of ultraviolet photogenerated current to dark current five times more than photoconductor fabricated using pristine ZnO nanoparticles [21]. Similarly, in a study by A. Bazargan et al. dimethylformamide was used to passivate the surface of the intrinsic ZnO nanoparticles [23].

Moreover, researchers have not given sufficient consideration towards the choice of precursor chemicals used for the chemical modification of intrinsic ZnO nanocrystals to ZnO/ZnS core–shell nanostructure. In the current study, we have investigated structural, morphological, optical and compositional properties of ZnO/ZnS core–shell nanostructure prepared using sodium sulphide and thioacetic acid. Interestingly parasitic defect emission of intrinsic ZnO nanocrystals was found to be eliminated, which key limiting factor for optoelectronic applications of ZnO nanocrystals.

2 Experimental procedure

ZnS/ZnO core–shell nanostructure has been synthesized via a two-step chemical conversion method as explained in the following sections.

## 2.1 Co-precipitation-assisted hydrothermal synthesis of ZnO nanocrystals

In a typical experiment, ZnO nanocrystals were synthesized using ethanolic solutions of zinc acetate $(Zn(CH_3COO)_2 \cdot 2H_2O)$ and sodium hydroxide (NaOH). 1 M solution of acetate salt of zinc in ethanol was refluxed continuously for four hours at a temperature of 70 °C. To maintain the stoichiometry, a 2 M ethanolic solution of sodium hydroxide was also made. As-prepared NaOH solution was added to Zn^{2+} solution under vigorous stirring at 40 °C for 5 h. The obtained colloidal solution was transferred to Teflon-lined hydrothermal autoclave. The hydrothermal autoclave was maintained at 50 °C for 12 h in a muffle furnace. The autoclave was allowed to cool naturally and the obtained powder was thoroughly washed with distilled water using a vacuum filtration system.

2.1.1 Chemical conversion of ZnO nanocrystals to ZnS/ZnO core–shell nanostructure using thioacetamide (TAA)

The as-synthesized ZnO nanocrystals and 0.2 M solution of thioacetamide (TAA) were dissolved in a minimum quantity of water. After vigorous stirring, the solution was kept in a hydrothermal autoclave system which was upheld at a temperature of 100 °C for six hours in the furnace. The resulting powder was thoroughly washed with distilled water using a vacuum filtration system. Sulphur ions released due to the decomposition of thioacetamide react with the surface of zinc oxide nanocrystals resulting in the formation of ZnS nuclei. As the reaction proceeds, a dense core of ZnS is produced at the outer surface of ZnO particles. Due to the concentration gradient of Zn^{2+} and S^{2-} ions in the solution, Zn^{2+} ions will diffuse outward towards the shell, whereas the S^{2-} ions will diffuse inwards towards the core as shown in Scheme 1. Such an effect is a consequence of the difference in diffusion rates of the metal atoms as suggested in the Kirkendall effect. Kirkendall effect is a process of mutual diffusion of chemical ions along two opposite directions under thermally activated conditions. By adding sulphide-based chemical conversion agents pristine ZnO nanocrystals, released S^{2-} ions in solution form a layer at the outer surface of ZnO, because diffusion rate of cation Zn^{2+} is more as compared to anions S^{2-}. The outward movement of Zn^{2+} ions is faster than the inward movement of S^{2-} ions, as a consequence of which size of ZnO core is consumed and growth of ZnS takes place [29]. Thioacetamide hydrolyses with water to form hydrogen sulphide gas via the following reaction [30].

$$CH_3CSNH_2 + H_2O \rightarrow CH_3CONH_2 + H_2S$$
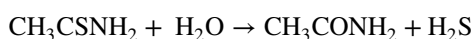
Hydrogen sulphide gas evolved readily reacts with ZnO nanocrystal surface to produce ZnS

$$ZnO + H_2S \rightarrow ZnS + H_2O$$
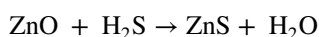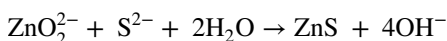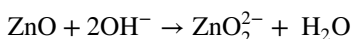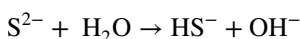
2.1.2 Chemical conversion of ZnO nanocrystals to ZnS/ZnO core–shell nanostructure using sodium sulphide (Na₂S)

As-grown ZnO nanoparticles were dissolved in 0.1 M zinc acetate solution at 60 °C for 30 min. After a vigorous stirring, 0.1 M solution of sodium sulphide nonahydrate $(Na_2S \cdot 9H_2O)$ was added dropwise. The subsequent precipitate was washed with distilled water and ethanol using vacuum filtration. The final product was dried in a muffle furnace to obtain the final powder. The possible reaction mechanism is explained as follows:
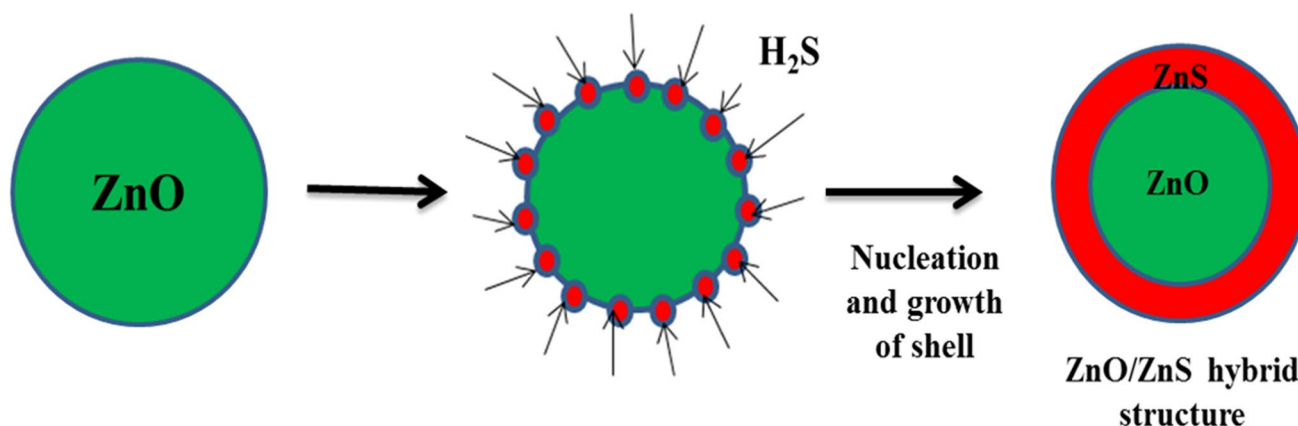
Scheme 1. Proposed mechanism towards the formation of ZnS shell over ZnO nanocrystal surface

$$S^{2-} + H_2O \rightarrow HS^- + OH^-$$

$$ZnO + 2OH^- \rightarrow ZnO_2^{2-} + H_2O$$

$$ZnO_2^{2-} + S^{2-} + 2H_2O \rightarrow ZnS + 4OH^-$$

2.2 Characterization tools

Structural characterization was carried out using powder X-ray powder diffraction (XRD) studies using X-ray diffractometer of make Bruker with Cu–Kα radiation (1.5406 Å) operated at 35 kV accelerating voltage. Microstructure images of the powder samples were studied using a scanning electron microscope of make: Zeiss, model Supra 40VP). Energy-dispersive X-ray spectroscopy (EDXS, model Oxford INCA 250) was used for elemental analysis of the as-prepared samples. UV-Visible studies were carried out using UV 2401PC, Shimadzu UV–Vis spectroscopy. Photoluminescence properties and defect analysis of the samples Edinburgh make luminescence spectrometer (model F900) fitted with a xenon lamp. Functional groups and other compositional analysis of the powder samples were studied using Fourier transform infrared spectroscopy of PerkinElmer spectrometer spectrum RX-I make at a resolution of 4 cm^{-1}. Electron paramagnetic resonance spectroscopy was recorded using Bruker Biospin make, model A300, X band.

3 Results and discussion

3.1 Powder X-ray diffraction (P-XRD) studies

Figure 1 represents the powder X-ray diffraction (P-XRD) pattern of ZnO nanocrystals prepared using the co-precipitation-assisted hydrothermal method. Diffraction peaks indicate the hexagonal wurtzite structure of ZnO nanocrystals. Peak broadening confirms that the size of as-grown ZnO particles falls in the nanoregime. Diffraction peaks were found to be consistent with standard data from JCDPS card file number 36-1451. Zn and O atoms in the ZnO wurtzite structure crystallize in a hexagonal closed pack structure, with each zinc atom being surrounded by four oxygen atoms, resulting in a tetrahedral non-centrosymmetric structure [31, 32]. No spurious or intermediate crystalline phases were observed, demonstrating the high crystalline purity of as-grown nanocrystals. The average crystallite size (D) in the as-grown nanocrystals was calculated to be ~30 nm using the Sherrer equation [33] given in Eq. 1.

$$D = \frac{b\lambda}{FWHM(2\theta)\text{Cos}\theta} \tag{1}$$

where FWHM is the full width at half maximum of the peaks in radian, θ is the Bragg angle or scattering angle and λ is the X-ray wavelength of Cu–Kα radiation (1.540 Å). b is constant whose value depends on shape and particle size distribution. The value of b was taken to be 0.94 for particles of nearly spherical particles. For polycrystalline materials, **D** is a measure of the volume-averaged crystallite size. Upon chemical conversion of as-grown ZnO nanocrystals, ZnS nuclei start forming at the surface of ZnO nanocrystals. As the reaction proceeds, more and more ZnS nuclei start getting attached to the surface of ZnO nanocrystals, resulting in the formation of the uniform shell over the ZnO nanocrystal surface. Figure 2 clearly shows the prominent peaks corresponding to (111), (220), (311) planes of the cubic phase of ZnS. Peaks of the ZnS were found to be well matching with the standard data card JCPDF: 005-0566. Along with ZnS peaks, additional peaks corresponding to (100), (002), (101) and (201) planes of ZnO nanocrystals were also found
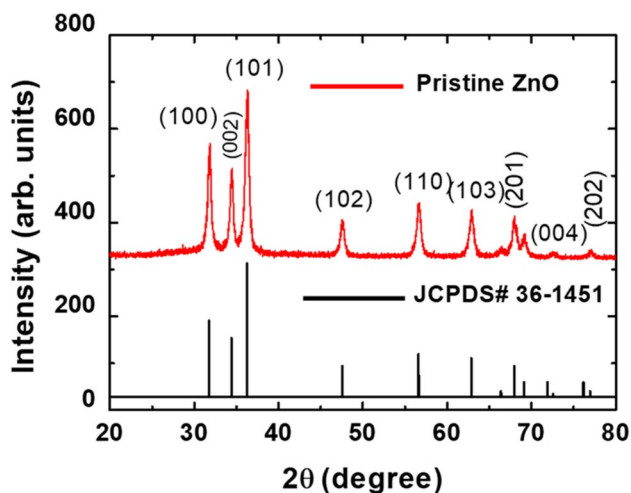
Fig. 1 a Powder X-ray diffraction pattern of as-prepared ZnO nanocrystals and **b** JCPDS card #00–036-1415 of intrinsic ZnO

which confirms the formation of ZnO/ZnS nanostructure. The average crystallite size of the ZnO/ZnS nanostructure synthesized using TAA and Na_2S as calculated using the Scherrer equation was found to be 13 and 10 nm, respectively. Further, no spurious impurity phases can be observed from the X-ray diffraction pattern.

3.2 Energy-dispersive X-ray spectroscopic analysis

Samples were studied for their elemental analysis using energy-dispersive X-ray spectroscopy (EDAX) attached with scanning electron microscope (SEM). EDAX

spectrum of pure ZnO nanocrystals, as shown in Fig. 3a, shows that the obtained nanocrystals are composed of Zn and O without any other impurities within the detection limits. As shown in Fig. 3a, b after the sulphidation reaction using thioacetamide and sodium sulphide, EDAX spectra clearly show the presence of sulphur in ZnO/ZnS nanostructure which confirms the successful suphidation process over ZnO nanocrystals. Further, unwanted or foreign elements were not detected from EDAX spectra.

3.3 Fourier transform infrared spectroscopy

Chemical bonding and interactions of as-prepared samples were studied obtained using FTIR spectroscopy analysis. FTIR allows the identification of various functional groups within a molecule. Any change in the molecular structure as a result of doping/contamination/composite formation can also be detected using FTIR peaks. It also gives information about the functional groups of surface dangling bonds if any. Figure 4a–c represents the FTIR spectra of the pristine ZnO nanocrystals and chemically converted ZnO nanocrystals using thioacetamide and sodium sulphide. A prominent band observed ~ 3357 cm^{-1} which represent the O–H stretching mode due to the presence of hydroxyl (OH) group was found in all the samples. Bands located within the range of ~ 2830–2920 cm^{-1} indicate C–H stretching mode [31], whereas band centred at ~ 2340 cm^{-1} region indicates the presence of absorbed CO_2. Prominent peak ~ 1410 cm^{-1} attributes OH bending and stretching vibration. In addition to these, low-intensity bands could be observed because the presence of surface hanging organic chemical groups such as H–O–H, CH_3COOH and CH can also be observed. A peak positioned at 420–500 cm^{-1} is a characteristic peak
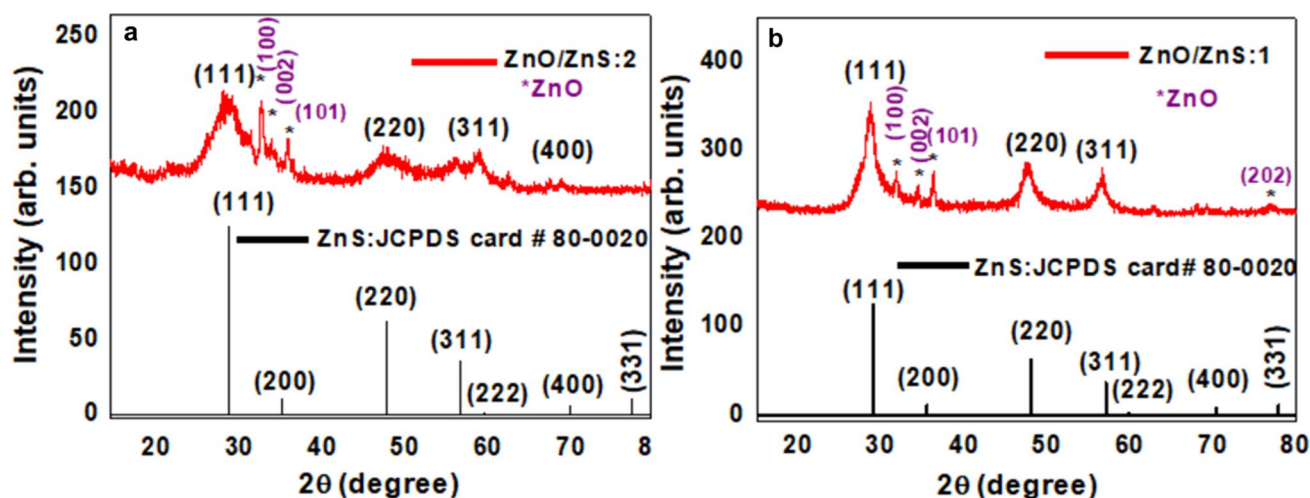
Fig. 2 Powder X-ray diffraction pattern of as-prepared ZnO/ZnS nanostructure via chemical conversion process using **a** thioacetamide, TAA and **b** Na_2S, respectively, and JCPDS card #00–080-0020 of intrinsic ZnS
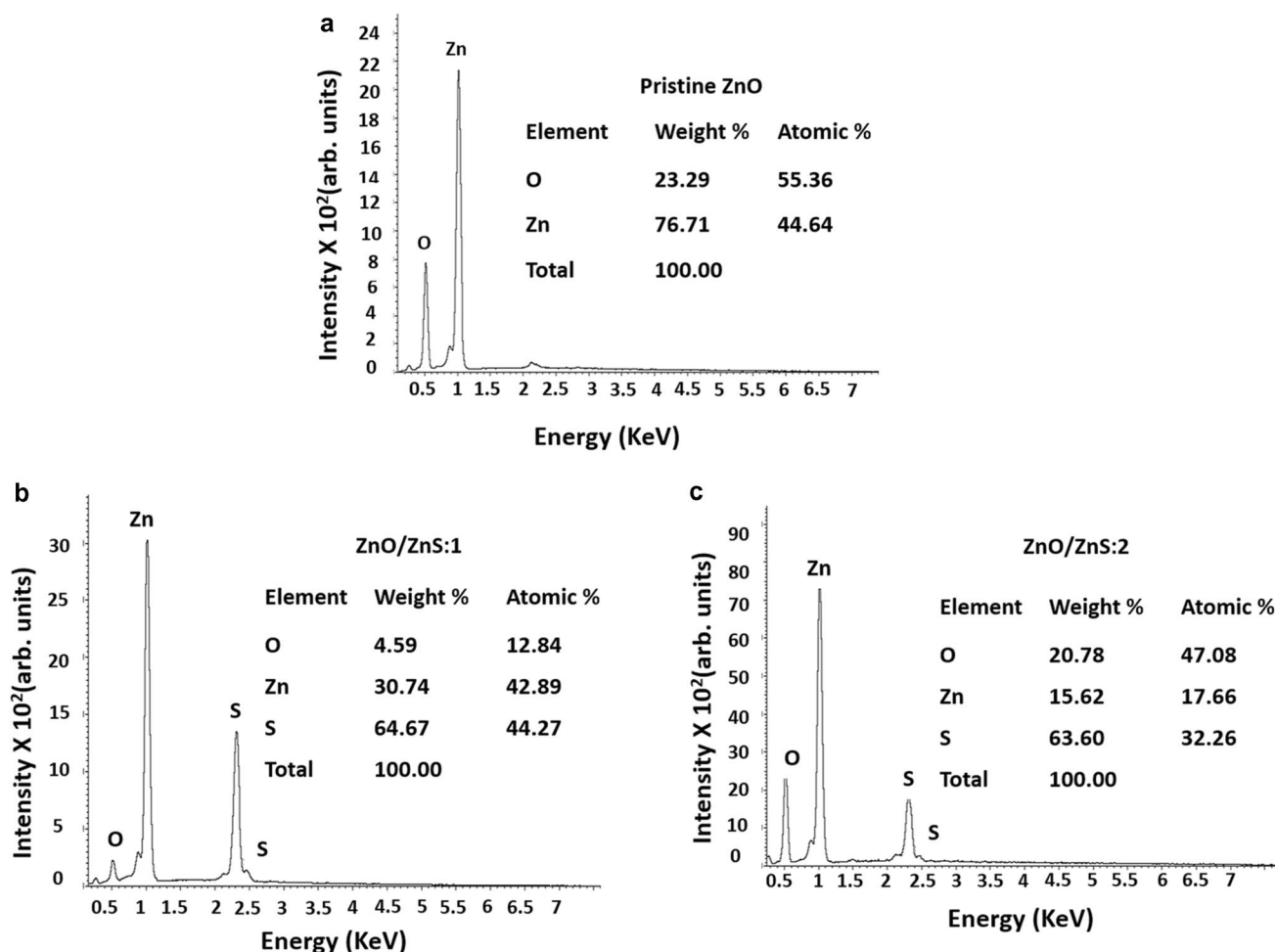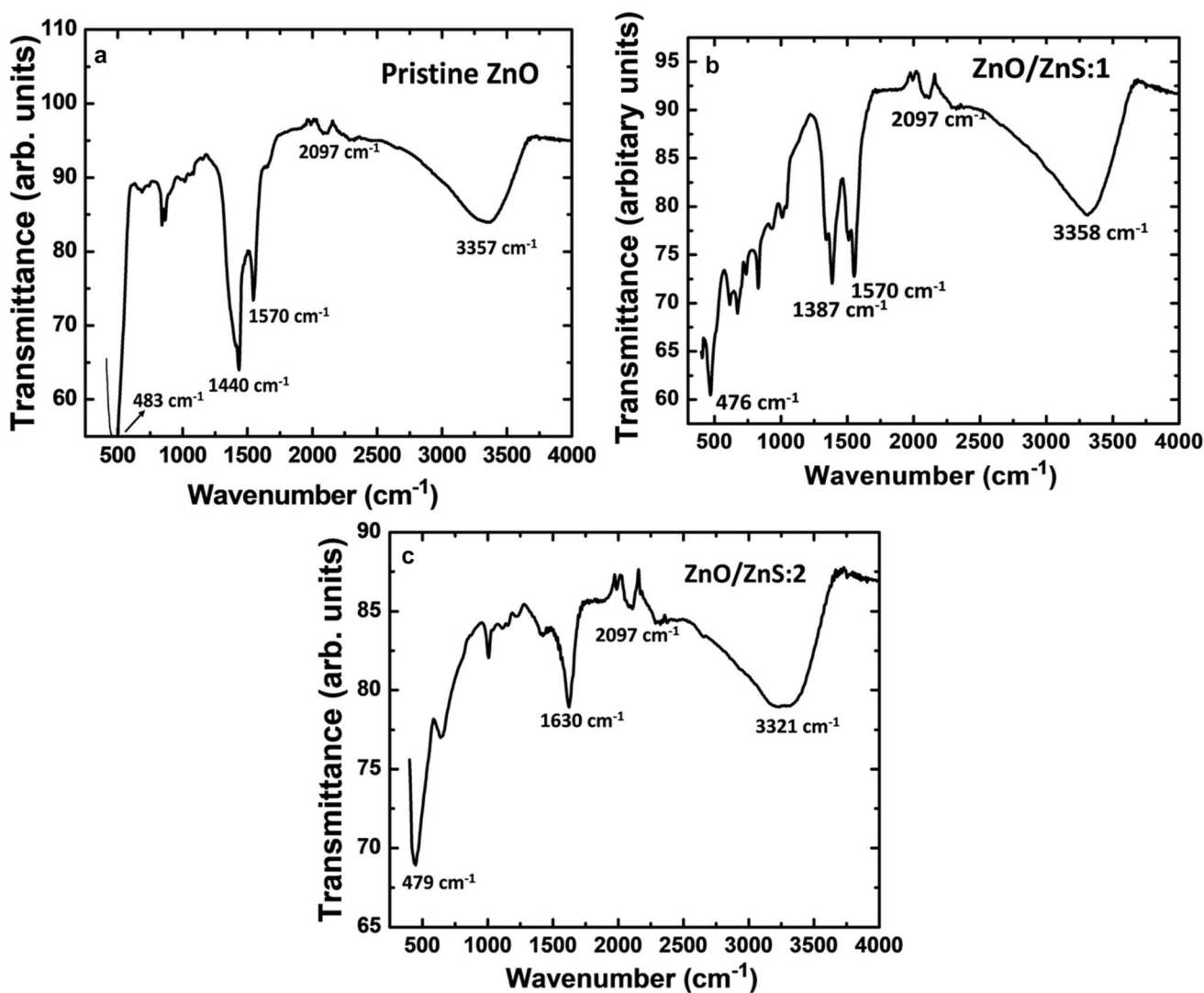
Fig. 3 EDAX spectra showing the composition information of as-prepared **a** ZnO nanocrystals, ZnO/ZnS nanostructure synthesized via chemical conversion with **b** TAA and **c** Na_2S, respectively

representing the vibrations of the Zn–O bond. Since peak position and its width depend on many critical parameters such as crystal structure, chemical composition and particle morphology, splitting of Zn–O band into multiple peaks was also observed and can be attributed to the irregular grain size of nanocrystals [32]. A slight depression in Zn–O-related band was observed in samples after the chemical conversion process, as shown in Fig. 4b, c which indicates due to the formation of the ZnS phase over ZnO nanocrystals. As shown in Fig. 4b, c, the intensity of the peaks around 3400 cm^{-1} is found to be augmented which suggest more OH groups are distributed on the surface of ZnO/ZnS nanostructure as compared to pristine ZnO nanocrystals. Increased absorption ability is attributed to interfacial roughness between ZnO and ZnS phases. Similar results were observed for ZnO/ZnS nanostructure synthesized using TAA and Na_2S, respectively.

3.4 Morphological analysis via SEM analysis

Microstructures images were recorded using SEM imaging to study the morphological properties of the as-prepared samples and to identify possible changes upon chemical conversion with thioacetamide and sodium sulphide, respectively. Figure 5a represents the morphology of intrinsic ZnO nanocrystals. Results indicate the formation of particles of nearly spherical morphology with small grain size. Owing to their small size and high surface-to-volume ratio, agglomeration in the particles can be observed from the micrographs. It is evident that due to agglomerating particles, clusters of nanoparticles are formed**.** Similar results were also observed by Ye et al. [34] and Ying et al. [35]. Figure 5b, c represents the morphology of the ZnO nanocrystals upon sulphurization with TAA and Na_2S, respectively. The darker regions of the core and relatively lighter regions of the shell consisting of a layer of nanoparticles on the surface of the core material can be seen. ZnS is found to grow and distribute uniformly

Fig. 4 FTIR spectra of as-prepared **a** ZnO nanocrystals, ZnO/ZnS nanostructure synthesized via chemical conversion with **b** TAA and **c** Na$_2$S, respectively

on the ZnO core surface because of the low atomic mobility at relatively lower synthesis temperature adapted in this current work.

3.5 UV–visible studies

To investigate the optical properties of the as-grown semiconductor and their core–shell structure, UV–Vis spectroscopic analysis was done. The band gap of the semiconductors can be calculated using the UV–Vis absorption spectra using the following relation in Eq. 2, known as Tauc's plot [36]:

$$(\alpha.h\vartheta)^{\frac{1}{\gamma}} = B\left(h\vartheta - E_g\right) \tag{2}$$

Factor α is the absorption coefficient, hυ is the photon energy, and B is a constant. γ factor depends on the nature of the electronic transition involved and is equal to 1/2 or 2 for the direct and indirect transition band gaps, respectively. Intrinsic ZnO nanocrystals show a band edge at ~ 3.39 eV, whereas the core–shell structure shows a substantial blue-shift in the absorption edge. Intrinsic ZnO does not show any considerable absorption in the visible region. By coating the intrinsic ZnO nanocrystals with ZnS, the effective band gap was found to be 3.47 eV and 3.44 eV using TAA and Na2S, respectively, as shown in Fig. 6. Inset in Fig. 6 represents the as recorded UV-Visible spectra of the intrinsic ZnO nanocrystals and ZnO/ZnS nanostructures. Intrinsic ZnO nanocrystals show an absorption edge at ~ 365 nm, which is very well consistent with the available literature [37].
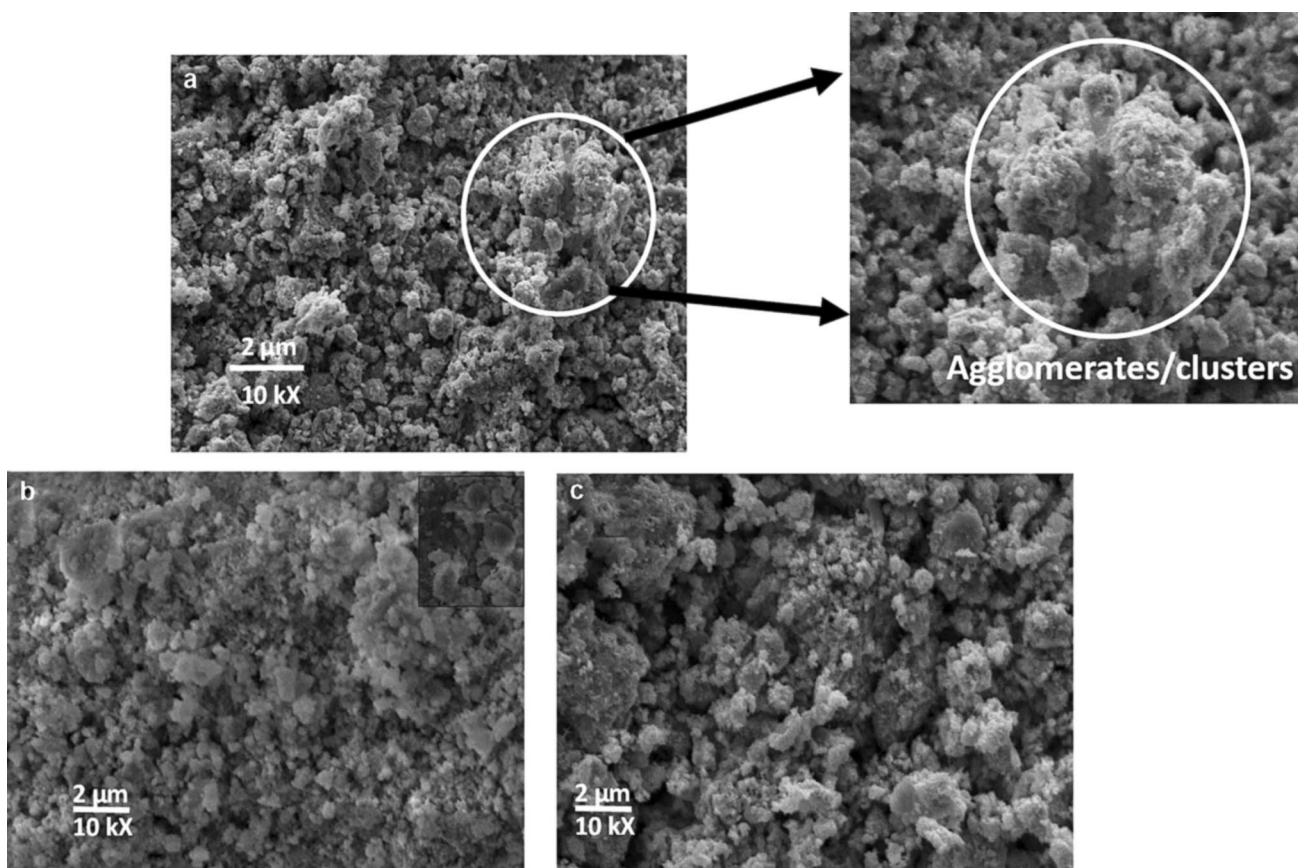
Fig. 5 SEM micrographs of as-prepared **a** ZnO nanocrystals, ZnO/ZnS nanostructure using chemical conversion agents: **b** TAA and **c** Na$_2$S, respectively

3.6 Photoluminescence studies

The room temperature photoluminescence (PL) emission spectrum was recorded and analysed to determine optical properties of as-grown ZnO nanocrystals before and after the process of sulphidation. Intrinsic ZnO nanocrystals exhibit band edge luminescence in the near UV region at ~ 380 nm and a broad emission peak in the visible region ~ 480–520 nm as shown in Fig. 7a [38, 39]. PL emission in UV region ~ 380 nm arises due to the radiative recombination of the charge carriers near the band edge of ZnO, whereas emission in visible region attributes to defect-related states. In most of the studies, coating of ZnS shell over ZnO has reported causing a blue-shift in the emission spectra of ZnO nanocrystal which was described based on Moss–Burstein effect, i.e. the effective band gap of ZnO semiconductor increases due to the formation of some additional donor energy states which are close to the conduction band of core semiconductor. Therefore, additional donor energy states populate the conduction band of ZnO pushing
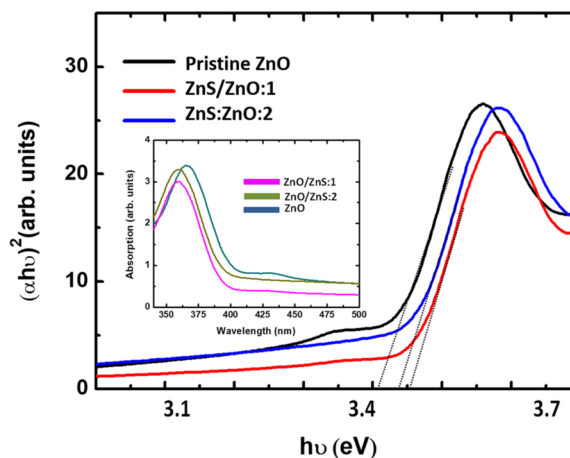

Fig. 6 Tauc's plot of $(\alpha h\nu)^2$ versus $h\nu$ for intrinsic ZnO nanocrystals and ZnO/ZnS nanostructures prepared using thioacetamide and Na$_2$S, respectively. Inset represents their corresponding UV–Vis spectra

the absorption edge to higher energy [40, 41]. However, interestingly, in this present study, the emission spectrum of ZnO/ZnS core/shell nanostructure shows a noticeable red-shift ~ 12 nm in UV emission peak as compared to that of intrinsic ZnO nanocrystals as shown in Fig. 7b, c. The red-shift of the UV emission peak can be ascribed to the strain caused due to the lattice mismatch between both semiconductors [42].

Different theories have been predicted for defect-related blue–green emission (480–520 nm) from the intrinsic ZnO nanocrystals by the researchers. Multiple factors such as the existence of singly ionized oxygen vacancies, zinc interstitials, multiple defect complexes and donor–acceptor complexes [43–45] have been reported. Some of the theories also suggest that apart from the defects, choice of the synthesis also plays a crucial role in manipulating the emission from

ZnO nanocrystals. Yong et al. have reported that during the hydrothermal synthesis process, excess oxygen ions in the precursor aqueous solution, may occupy interstitial sites of the ZnO crystal structure, thereby forming negatively charged interstitial oxygen ion which results in green emission ~ 510 nm [27]. Upon sulphidation, ZnO/ZnS core/shell nanostructure exhibits improved UV emission and defect-related blue–green emission was found to be suppressed to a large extent which indicates that the ZnS layer helps in passivating the surface of ZnO nanocrystals. Enhancing the UV sensitivity of ZnO nanocrystals has been a topic of research across the globe, especially for optoelectronic applications. ZnS layer suppresses the tunnelling of the electrons/holes from the core to un-passivated surface sites on the surface of the ZnO core [46]; thus, more photogenerated electrons and holes can be limited in the core of the ZnO
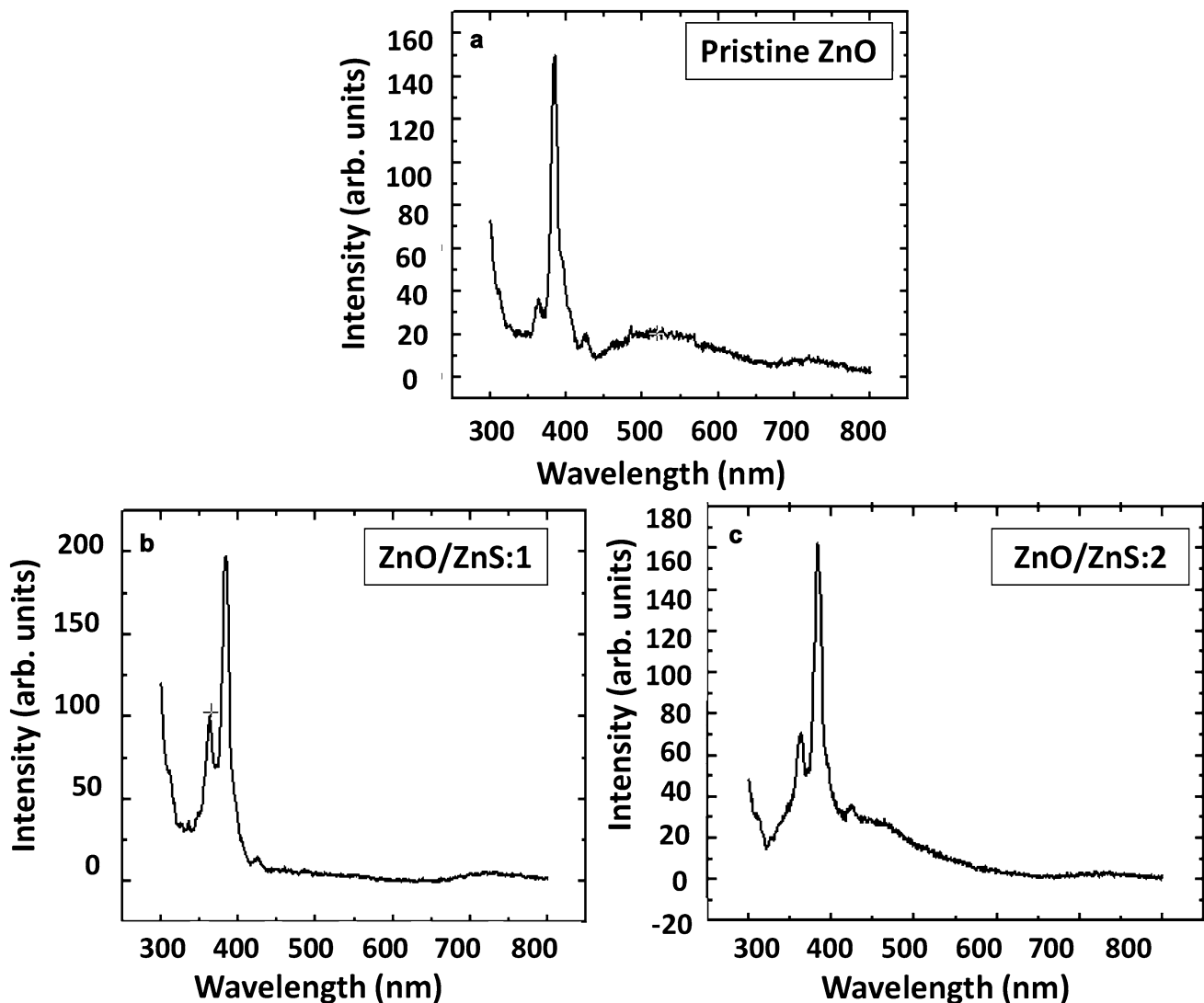
Fig. 7 Photoluminescence emission of as-prepared **a** ZnO nanocrystals and ZnO/ZnS nanostructure prepared using chemical conversion agents **b** TAA and **c** Na_2S, respectively

semiconductor, thus increasing the probability of radiative transitions in ZnO core. Thus, a wider band gap semiconductor (ZnS) passivates the surface dangling bonds present on the core of ZnO, resulting in an obvious enhancement in the UV luminescence. The drastic reduction or rather diminishing defect-mediated green luminescence indicates that the existence of fewer oxygen vacancies and zinc interstitials due to the presence of passivating shell of ZnS of considerable thickness. Thus ZnO/ZnS core/shell nanostructure potential shrinks non-radiative pathways and enhancing radiative recombination. ZnO/ZnS core/shell nanostructure prepared using TAA eliminates defect-related emission of ZnO as compared to sample made using Na2S, which shows a low-intensity shoulder peak at ~ 405 nm. Results confirm that ZnO/ZnS core/shell nanostructure has charge confinement in the core and shell region and thus has the type I characteristics of band alignment. ZnO/ZnS nanostructure thus finds many interesting applications in modern optoelectronic devices which require highly narrowband emission in UV region such as UV photodetectors, UV index monitoring devices, piezoelectric energy harvesting devices and UV light-emitting diodes.

3.7 Electron paramagnetic resonance (EPR) analysis

To understand the role of paramagnetic defects, electron paramagnetic resonance spectroscopy is a versatile and non-destructive characterization technique based on Zeeman splitting. It can be used to probe electron spin dynamics and magnetic defects/impurity analysis. Figure 8 shows the EPR spectra of intrinsic ZnO nanocrystals and ZnO/ZnS core–shell structure. Origin of EPR signal in zinc oxide semiconductor in the region of 1.94 -1.99 is still an issue of debate; however, most of the theories suggest that the origin of paramagnetic response in ZnO is attributed to surface defects such doubly charged zinc vacancies, neutral zinc interstitials, singly charged zinc interstitial, neutral oxygen vacancies, singly charged oxygen vacancy, complex of an oxygen vacancy and zinc interstitial type defects in ZnO [47–49]. Interestingly, ZnO/ZnS core–shell nanostructures samples did not show any EPR signal, which again proves that the layer of ZnS passivates the surface dangling. bonds and defects, thereby reducing the EPR signal which was originating from the surface defects. Also since defect-free
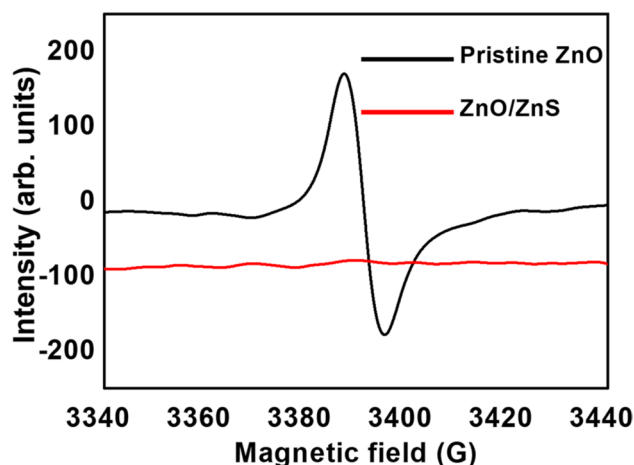

Fig. 8 EPR spectra of as-prepared ZnO nanocrystals and ZnO/ZnS nanostructure

ZnO is antiferromagnetic in nature [50] no significant signal can be recorded.

4 Conclusion

Type I core–shell nanostructure of ZnO/ZnS has been efficaciously prepared through a simplistic two-step sulphurization process using TAA and Na2S. Particles were found to have nearly spherical morphology with an average particle size of ~ 50 nm. Enhancement of near UV emission and suppression of defect-related luminescence in ZnO nanocrystals due to coating larger band gap ZnS was observed, which was also confirmed via EPR analysis. FTIR studies clearly show the enhanced OH absorption ability of core–shell nanostructure due to interfacial roughness between ZnO/ZnS. Table 1 compares some of the strikingly distinct properties which have been observed in ZnO/ZnS core–shell nanostructures synthesized in this present work as compared to previously reported work from the literature. As-prepared ZnO/ZnS nanostructures find many interesting applications in modern optoelectronic devices which require enhanced UV light emission without parasitic defects. Though the present work focuses on ZnO–ZnS-based core/shell nanostructure, other semiconductor core/shell structures are expected to be synthesized using the same procedure.

Table 1 Comparison of properties between as-synthesiesd ZnO/ZnS nanostructure with the ZnO/ZnS nanostructure reported in the literature

S. No	Properties	As-prepared sample	As per the literature	References
1	Photoluminescence properties	Red-shift ~ 12 nm in the emission peaks was observed in both samples prepared using Na_2S and TAA	Blue-shift was observed (~ 5 nm)	[51–54]
2	Defect states	Defect emission in visible region is completely eliminated	Slight decrease has been observed	[51–54]
3	Morphology	Nearly spherical particles with agglomeration	Rod-shaped particles were observed	[53, 54]
4	Heterostructure type	Type I	Type II	[55]

Declarations

Conflict of interest Authors G. Swati and Manoj Morampudi hereby declare they have no conflict of interest.

References

1. J. Chang, E.R. Waclawik, RSC Adv. **4**, 23505 (2014)
2. M.-R. Gao, Y.-F. Xu, J. Jiang, S.-H. Yu, Chem. Soc. Rev. **42**, 2986 (2013)
3. P. Reiss, M. Protiere, L. Li, Small **5**, 154 (2009)
4. S. Saha, P. Sarkar, Chem. Phys. Lett. **555**, 191 (2013)
5. S.K. Shaikh, V.V. Ganbavle, S.I. Inamdar, K.Y. Rajpure, RSC Adv. **6**, 25641 (2016)
6. S. Choi, A.M. Berhane, A. Gentle, C. Ton-That, M.R. Phillips, I. Aharonovich, ACS Appl. Mater. Interfaces **7**, 5619 (2015)
7. S.I. Inamdar, V.V. Ganbavle, K.Y. Rajpure, Superlattice Microst. **76**, 253 (2014)
8. M.M. Ismail, W.Q. Cao, M.D. Humadi, Optik **127**, 4307 (2016)
9. H.W. Kang, J. Leem, S.Y. Yoon, H.J. Sung, Nanoscale **6**, 2840 (2014)
10. P. Uthirakumar, C.-H. Hong, E.-K. Suh, Y.-S. Lee, Chem. Mater. **18**, 4990 (2006)
11. P.K. Vabbina, R. Sinha, A. Ahmadivand, M. Karabiyik, B. Gerislioglu, O. Awadallah, N. Pala, ACS Appl. Mater. Interfaces **23**, 19791 (2017)
12. B.G. Gerislioglu, L. Dong, A. Ahmadivand, H. Hu, P. Nordlander, N.J. Halas, Nano Lett. **20**, 2087 (2020)
13. A. Yadav, B. Gerislioglu, A. Ahmadivand, A. Kaushike, G.J.C.Z. Ouyang, Q. Wangh, V.S. Yadav, Y.K. Mishra, Y. Wu, Y. Liu, S.R. Krishna, Nano Today **37**, 101072 (2021)
14. S. Venkataprasad Bhat, S.R.C. Vivekchand, A. Govindaraj, C.N.R. Rao, Solid State Commun. **149**, 510 (2009)
15. L. Qin, C. Shing, S. Sawyer, P.S. Dutta, Opt. Mater. **33**, 359 (2011)
16. Y. Gong, T. Andelman, G.F. Neumark, S. O'Brien, I.L. Kuskovsky, Nanoscale Res Lett. **2**(6), 297 (2007)
17. H.S. Kang, J.S. Kang, J.W. Kim, S.Y. Lee, J. Appl. Phys. **95**, 1246 (2004)
18. S.B. Zhang, S.-H. Wei, A. Zunger, Phys. Rev. B **63**, 075205 (2001)
19. D.C. Reynolds, D.C. Look, B. Jogai, J. Appl. Phys. **89**, 6189 (2001)
20. K. Grieve, P. Mulvaney, F. Grieser, Curr. Opin. Colloid Interface Sci. **5**, 168 (2000)
21. D.C.J. Neo, C. Cheng, S.D. Stranks, S.M. Fairclough, J.S. Kim, A.I. Kirkland, J.M. Smith, H.J. Snaith, H.E. Assender, A.A.R. Watt, Chem. Mater. **26**, 4004 (2014)
22. S. Sawyer, L. Qin, C. Shing, Zinc oxide nanoparticles for ultraviolet photodetection. Int. J. High Speed Electron. Syst. **20**, 183 (2012)
23. A.M. Bazargan, F. Sharif, S. Mazinani, N. Naderi, J Mater Sci: Mater Electron **27**, 8221 (2016)
24. P. Singh, B. Rajesh, S. Bishnoi, G. Swati, V.V. Jaiswal, V. Shanker, D. Haranath, Ceram. Int. **42**, 17016 (2016)
25. Hu. Linfeng, M.M. Brewster, Xu. Xiaojie, C. Tang, S. Gradečak, X. Fang, Nano Lett. **13**, 1941 (2013)
26. G. Malloci, L. Chiodo, A. Rubio, A. Matton, J. Phys. Chem. C **116**, 8741 (2012)
27. S.K. Kailasa, H.-F. Wu, Analyst **135**, 1115 (2010)
28. S.K. Kailasa, K. Kiran, H.-F. Wu, Anal. Chem. **80**, 9681 (2008)
29. X.M. Shuai, W.Z. Shen, J. Phys. Chem. C **6415**, 115 (2011)
30. Y. Hu, H. Qian, Y. Liu, G. Du, F. Zhang, L. Wang, X. Hu, CrystEngComm **13**, 3438 (2011)
31. C.-C. Cheng, C.-F. Cho, J.L. Chiu, C.-T. Tsai, H. Chen, Results Phys. **10**, 449 (2018)
32. E. Júnior, F. Nobre, G. Laécio, S. Cavalcante, M. Santos, F. Souza, J.M. Matos, RSC Adv. **7**, 24263 (2017)
33. G. Swati, D. Bidwai, D. Haranath, Nanotechnology **31**, 364007 (2020)
34. Y. Ye, H. Zhang, Y. Chen, P. Denga, Z. Huang, L. Liu, Y. Qian, Y. Li, Q. Li et al., J Alloy Compd. **639**, 422 (2015)
35. Y.P. Xie, Z.B. Yu, G. Liu, X.L. Ma, H.-M. Cheng, Energy Environ. Sci. **7**, 1895 (2014)
36. P. Makuła, M. Pacia, W. Macyk, J. Phys. Chem. Lett. **9**(23), 6814–6817 (2018)
37. P. Fageria, S. Gangopadhyay, S. Pande, RSC Adv. **4**, 24962 (2014)
38. G. Rani, P.D. Sahare, Nano Commun. Netw. **3**, 197–202 (2012)
39. H. Kleinwechter, C. Janzen, J. Knipping, H. Wiggers, P. Roth, J. Mater. Sci. **37**, 4349 (2002)
40. E.M. Flores, C.W. Raubach, R. Gouvea, E. Longo, S. Cava, M.L. Moreira, Optical and structural investigation of ZnO@ZnS core–shell nanostructures. Mater. Chem. Phys. **173**, 347 (2016)
41. M. Sookhakian, Y.M. Amin, W.J. Basirun, M.T. Tajabadi, N. Kamarulzaman, Synthesis, structural, and optical properties of type-II ZnO–ZnS core–shell nanostructure. J. Lumin. **145**, 244 (2014)
42. K.S. Ranjith, A. Senthamizhan, B. Balusamy, T. Uyar, Catal. Sci. Technol. **7**, 1167 (2017)
43. G. Swati, S. Mishra, D. Yadav, R.K. Sharma, D. Dwivedi, N. Vijayan, J.S. Tawale, V. Shanker, D. Haranath, J. Alloys Comp. **571**, 1 (2013)
44. R. Khokhra, B. Bharti, H.-N. Lee, R. Kumar, Sci Rep. **7**, 15032 (2017)

45. P. Camarda, F. Messina, L. Vaccaro, S. Agnello, G. Buscarino, R. Schneider, R. Popescu, D. Gerthsen, R. Lorenzi, F. Gelardi, M. Cannas, Phys. Chem. Chem. Phys. **18**, 16237 (2016)

46. G. Hitkari, S. Singh, G. Pandey, Nano-Struct. Nano-Objects **12**, 1 (2017)

47. D. Savchenko, A. Vasin, O. Kuz, I. Verovsky, A. Prokhorov, A. Nazarov, J. Lančok, E. Kalabukhova, Sci. Rep **10**, 17347 (2020)

48. E. Cerrato, M.C. Paganini, E. Giamello, J. Photochem. Photobiol **397**, 112531 (2020)

49. M. Kakazey, M. Vlasova, M. Dominguez-Patiño, M. Dominguez-Patiño, G. Srećković, T.N. Natalija, Sci. Sinter. **36**, 65 (2004)

50. H.-L. Guo, Q. Zhu, X.-L. Wu, Y.-F. Jiang, X. Xie, A.-W. Xu, Nanoscale **7**, 7216 (2015)

51. S.-T. Tai, Y.-S. Tsai, Y.C. Sermon Wu, W. J.-Jr. Wang, C. Hsiang, Results Phys. **15**, 102703 (2019). https://doi.org/10.1016/j.rinp.2019.102703

52. M. Sookhakian, Y.M. Amin, W.J. Basirun, M.T. Tajabadi, N. Kamarulzaman, J. Lumin. **145**, 244 (2014)

53. Y.-C. Liang, C.-C. Wang, RSC Adv. **8**, 5063 (2018)

54. X.M. Shuai, W.Z. Shen, J. Phys. Chem. C **115**, 6415–6422 (2011)

55. M.A. Hassan, M.A. Johar, A. Waseem, I.V. Bagal, J.-S. Ha, S.-W. Ryu, Opt. Express **27**, A184–A196 (2019)